ADVANCED ELECTRONIC MATERIALS
www.advelectronicmat.de

Dysprosium Iron Garnet Thin Films with Perpendicular Magnetic Anisotropy on Silicon

Jackson J. Bauer, Ethan R. Rosenberg, Subhajit Kundu, K. Andre Mkhoyan, Patrick Quarterman, Alexander J. Grutter, Brian J. Kirby, Julie A. Borchers, and Caroline A. Ross**

Magnetic insulators, such as the rare-earth iron garnets, are promising materials for energy-efficient spintronic memory and logic devices, and their anisotropy, magnetization, and other properties can be tuned over a wide range through selection of the rare-earth ion. Films are typically grown as epitaxial single crystals on garnet substrates, but integration of these materials with conventional electronic devices requires growth on Si. The growth, magnetic, and spin transport properties of polycrystalline films of dysprosium iron garnet (DyIG) with perpendicular magnetic anisotropy (PMA) on Si substrates and as single crystal films on garnet substrates are reported. PMA originates from magnetoelastic anisotropy and is obtained by controlling the strain state of the film through lattice mismatch or thermal expansion mismatch with the substrates. DyIG/Si exhibits large grain sizes and bulk-like magnetization and compensation temperature. Polarized neutron reflectometry demonstrates a small interfacial nonmagnetic region near the substrate. Spin Hall magnetoresistance measurements conducted on a Pt/DyIG/Si heterostructure demonstrate a large interfacial spin mixing conductance between the Pt and DyIG comparable to other garnet/Pt heterostructures.

1. Introduction

Thin films of the archetypical yttrium iron garnet ($Y_3Fe_5O_{12}$,YIG) and rare-earth iron garnets ($RE_3Fe_5O_{12}$, REIG) have attracted considerable attention recently for studies of spin torques,[1–4] spin waves,[5–8] and magneto-optical effects.[9–11] Selection of the rare-earth ion enables tuning of the saturation magnetization,[12,13] magnetocrystalline anisotropy,[14] magnetostriction,[15] Gilbert damping parameter,[16–19] and magnetooptical spectral response,[10,20,21] and the net anisotropy may be varied widely by choice of substrate, which affects the strain state of the film.[22,23] Ferrimagnetic insulators, such as YIG and REIG, are particularly promising for spintronics as they do not contribute Ohmic losses from parasitic current shunting and exhibit fast magnetization dynamics and low losses in the THz regime.[24] Films with perpendicular magnetic anisotropy (PMA) are advantageous for investigation of spin-orbit torque (SOT) effects, chiral magnetic textures such as skyrmions, and for high density information storage based on domain walls.[25,26] It is difficult to grow YIG with PMA, but REIG films with PMA have been grown, and manipulation of their magnetization has been demonstrated via a spin-orbit torque (SOT) from an adjacent heavy metal[3,27] or from a topological insulator[28,29] with a large spin Hall angle. Electrical control of the magnetization using the damping-like SOT offers the potential for memory and logic devices with ultra-low power dissipation.[30–32] Taking advantage of these properties in spintronic devices requires the integration of PMA REIG films onto non-garnet substrates; silicon is of particular interest as a substrate due to its commercial ubiquity.

Single crystal garnet thin films have been grown with PMA by selecting a substrate and garnet composition such that the out-of-plane magnetoelastic anisotropy K_{me} originating from epitaxial lattice mismatch overcomes the shape anisotropy K_{sh}. PMA has been demonstrated in samarium-,[33] thulium-,[18] europium-,[19,34] and terbium[19,34] iron garnets on gadolinium gallium garnet ($Gd_3Ga_5O_{12}$, GGG) substrates, and bismuth-substituted yttrium-[7] and thulium-[35,36] iron garnets on substituted GGG ($Gd_{2.6}Ca_{0.4}Ga_{4.1}Mg_{0.25}Zr_{0.65}O_{12}$, SGGG). For films grown on (111)-oriented garnet substrates the magnetocrystalline anisotropy also contributes to PMA by an amount $K_1/12$, which is typically small, where K_1 is the first order magnetocrystalline anisotropy coefficient.

For polycrystalline films grown on non-garnet substrates, the elastic anisotropy originates instead from thermal expansion mismatch with the substrate on cooling from the annealing

J. J. Bauer, E. R. Rosenberg, Prof. C. A. Ross
Department of Materials Sciences and Engineering
Massachusetts Institute of Technology
77 Massachusetts Ave, 13-4017, Cambridge, MA 02139, USA
E-mail: bauerj@mit.edu; caross@mit.edu
Dr. S. Kundu, Prof. K. A. Mkhoyan
Department of Chemical Engineering and Materials Science
University of Minnesota – Twin Cities
421 Washington, Ave. SE, Minneapolis, MN 55455, USA
Dr. P. Quarterman, Dr. A. J. Grutter, Dr. B. J. Kirby, Dr. J. A. Borchers
NIST Center for Neutron Research
100 Bureau Drive, Gaithersburg, MD 20899, USA
The ORCID identification number(s) for the author(s) of this article can be found under https://doi.org/10.1002/aelm.201900820.

DOI: 10.1002/aelm.201900820

temperature used to crystallize the films after growth.[20,23,37] Considerable work was done on thin film polycrystalline REIGs for bubble memory in the 1960–1970s, where PMA was promoted by lowering the magnetization and therefore the shape anisotropy (e.g., by Al or Ga substitution for Fe), and from a growth-induced anisotropy.[38,39] Recently PMA was achieved in polycrystalline films of europium iron garnet (EuIG) on (0001) quartz,[23] $Dy_{3-x}Bi_xFe_{5-y}Ga_yO_{12}$ on glass,[40] and for $Dy_{3-x}Ce_xFe_{5-y}Al_yO_{12}$ on Si[41] due to a dominant magnetoelastic anisotropy. A mixed anisotropy has also been reported for $Gd_3Fe_5O_{12}$ on Si.[42] To obtain PMA, a combination of positive (negative) magnetostriction and an in-plane compressive (tensile) strain state is required. Since iron garnets have a relatively high thermal expansion coefficient (e.g., 10.4 10^{-6} K^{-1} for YIG[43]), the garnet will be under in-plane tensile strain on many common substrates after annealing, with the exception of high thermal expansion materials such as (0001)-oriented quartz.[44] There has not been a demonstration of a REIG with PMA on Si without Fe-site substitution.

To obtain a PMA REIG on Si, we select dysprosium iron garnet (DyIG) which has large and negative magnetostriction constants λ_{100} and λ_{111}[15] at room temperature, favoring PMA when the film is under sufficient in-plane tensile stress.[45] Dysprosium has historically been substituted into garnets and other oxides to enhance the saturation magnetostriction and the magneto-optical response.[46,47] Bulk, stoichiometric DyIG crystals have also undergone extensive study to characterize their complex non-collinear magnetic structure in large fields and at cryogenic temperatures.[48–51] Electrical transport in DyIG and Sr-substituted DyIG has been examined for use in phase shift and microwave applications.[52,53] The Faraday rotation and magnetic circular dichroism of Bi- and Sc-substituted DyIG have also been widely studied.[20,41,54,55] Despite this large body of work on the bulk and magneto-optical properties of Dy-containing garnets, the spintronic applications of this material have yet to be explored.

The aim of this study is to demonstrate growth and spintronic properties of a polycrystalline REIG, DyIG, which exhibits PMA on a silicon substrate without Fe-site substitution. We compare the structural and magnetic properties of polycrystalline DyIG on Si with those of single crystal DyIG on garnet substrates. The polycrystalline films consist of single phase garnet having large grains sizes on the order of 10 μm in ≈40 nm thick films and exhibit a tensile thermal mismatch strain, whereas the single crystal films are coherently strained to match the garnet substrate lattice parameter and are under tensile or compressive strain depending on the substrate composition. Spin Hall magnetoresistance measurements on Pt/DyIG/Si heterostructures indicate spin mixing conductance at the Pt/DyIG interface comparable to that of Pt/YIG, Pt/TmIG, and Pt/EuIG. These results demonstrate the utility of DyIG in spintronic devices on a Si platform.

2. Epitaxial DyIG Films

Films were grown by pulsed laser deposition (PLD) in the presence of oxygen from a stoichiometric DyIG target onto substrates held at an elevated temperature. Single crystal films were grown on GGG, SGGG, and GSGG ($Gd_3Sc_2Ga_3O_{12}$) in (111) orientations to modify the epitaxial lattice mismatch. The cubic lattice parameters were 1.2376 nm for GGG, 1.2480 nm for SGGG, and 1.2554 nm for GSGG. The Methods section provides further details of film growth.

The high-resolution X-ray diffraction (HRXRD) scans of the (444) reflection of single crystal DyIG films on (111) GGG, SGGG, and GSGG are shown in **Figure 1**a. The high crystalline quality is evidenced by the distinct film peak and the Laue fringes. Prior work on REIG grown on garnet substrates shows that the REIG grows coherently on the substrate, matching its in-plane lattice parameter.[18] For (111) films the DyIG cubic unit cell is in a state of pure shear strain leading to a rhombohedral distortion. The DyIG films grown on GGG are under in-plane compression and the films on SGGG and GSGG are under in-plane tension. The unit cell volume of the DyIG films, V = 1.9164, 1.8966, and 1.8856 nm^3, on GGG, SGGG, and GSGG respectively, decreases with increasing in-plane tension; for comparison the bulk lattice parameter of DyIG is 1.2405 nm[3][56] (V = 1.9089 nm^3).

Vibrating sample magnetometer (VSM) hysteresis loops are shown in Figure 1b. The DyIG/GGG film has the lowest coercivity $\mu_0 H_c \approx 1$ mT and its saturation magnetization M_s was 50 kA m^{-1}. $\mu_0 H_c \approx 5$ mT and M_s = 50 kA m^{-1} for DyIG/SGGG and $\mu_0 H_c \approx 5$ mT and M_s = 30 kA m^{-1} for DyIG/GSGG. The DyIG grown on GGG demonstrates an IP easy axis whereas the films on SGGG and GSGG exhibit PMA.

The easy axis orientation is attributed to the magnetoelastic anisotropy, which is the dominant contribution to the net uniaxial anisotropy of the (111)-oriented single crystal film, $K_{u,sc}$ given by[18]

$$K_{u,sc} = -\frac{K_1}{12} + \frac{9}{4}\lambda_{111}c_{44}\left(\frac{\pi}{2} - \beta\right) + \frac{\mu_0}{2}M_s^2 \quad (1)$$

where K_1 is the first order magnetocrystalline anisotropy, < −500 J m^{-3}[14]; λ_{111} the magnetostriction, -5.9×10^{-6}[15]; c_{44} the shear modulus, 76.4 GPa for YIG[57]; β the corner angle of the rhombohedrally distorted unit cell, and M_s the saturation magnetization, ≈30 kA m^{-1} for bulk DyIG at room temperature.[58] Comparing the bulk lattice parameter of DyIG with that of the substrates, the lattice mismatch is 0.23%,[56] −0.60%, and −1.19% for DyIG on GGG, SGGG, and GSGG respectively, that is, with a negative λ_{111} the magnetoelastic anisotropy favors an in-plane easy axis for DyIG/GGG and out-of-plane easy axis for DyIG/SGGG and DyIG/GSGG, as observed.

The film out-of-plane lattice parameter and rhombohedral cell corner angle determined from the HRXRD scans[18,19] yield β = 89.7°, 90.4°, and 90.8° for DyIG on GGG, SGGG, and GSGG respectively. From the bulk value of the magnetostriction constant, λ_{111}, we use Equation[1] to estimate the hard axis anisotropy field $\mu_0 H_k = 2\ K_{u,sc}/M_s$ = 190 mT (where the hard axis is out of plane) for DyIG/GGG and 80 and 240 mT (in plane hard axis) for DyIG on SGGG and GSGG, respectively. However, experimentally the hard axis saturation field was higher than 1.2 T, the limit of the VSM. This suggests that the magnetostriction constant of DyIG films is greater than the bulk value, due, for example, to non-bulk stochiometry or film heterogeneities.[19,59]

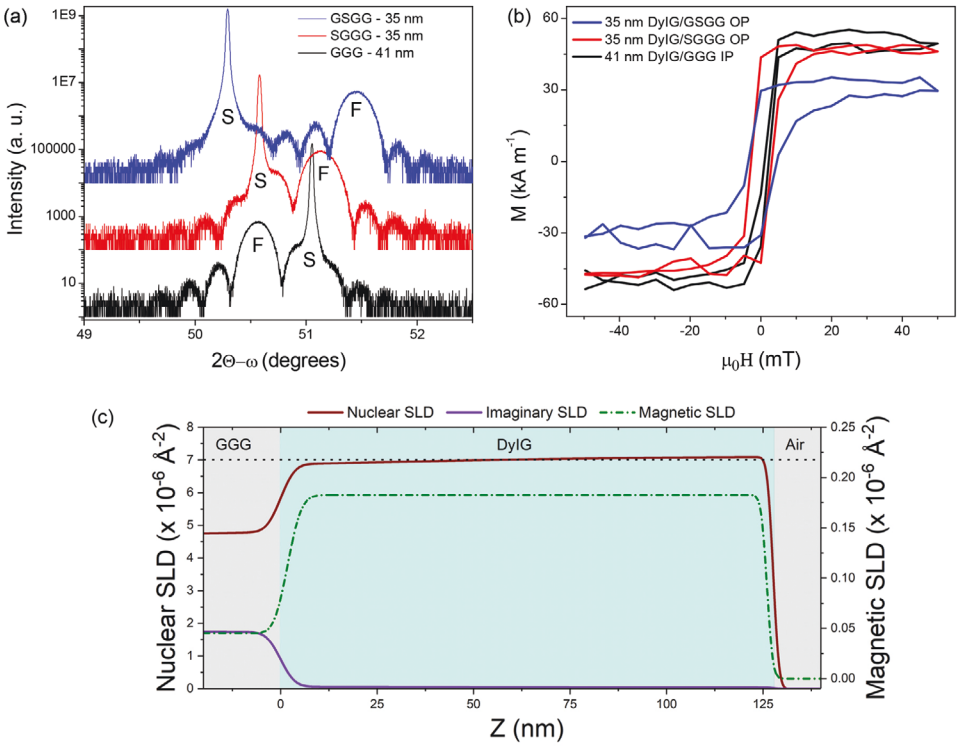

Figure 1. a) HRXRD scans of DyIG/GGG, DyIG/SGGG, and DyIG/GSGG films (vertically offset for clarity with film and substrate peaks labeled F and S, respectively). b) VSM hysteresis loops of the easy axes of the single crystal DyIG films. An in-plane (IP) loop is shown for DyIG/GGG and out-of-plane (OP) loops are shown for DyIG/SGGG and DyIG/GSGG. c) The nuclear (red, solid), imaginary SLD (purple, solid), and magnetic (green, dashed) scattering length densities (SLD) as a function of depth as determined from fitting PNR data (see Figure S2, Supporting Information), where $z = 0$ nm refers to the surface of the GGG substrate. The black dotted line denotes the bulk SLD of DyIG.

Temperature-dependent VSM measurements were conducted to determine the compensation temperature of a bulk DyIG reference sample and a DyIG/GGG thin film sample, shown in **Figure 2**. Bulk DyIG has a magnetic compensation temperature near 220 K,[13,60] and our bulk sample, which was made by sintering of ceramic powders in the same manner as the PLD target, shows a compensation temperature in good agreement with the literature value. However the DyIG/GGG film shows a compensation temperature of ≈190 K, about 30 K below the bulk value. As previously described by Rosenberg et al. for TbIG,[19] this difference may indicate a non-ideal stoichiometry or non-bulk site occupancy in the films.

In-plane ferromagnetic resonance (FMR) measurements were conducted on a 116 nm DyIG/GGG sample from 3–5 GHz in an electromagnet with a maximum field of 400 mT. The film had $M_s = 60$ kA m^{-1} and $\mu_0 H_c \approx 0.2$ mT, as shown in Figure S1, Supporting Information. Numerous studies[18,19] have shown that the presence of rare-earth ions greatly increases the Gilbert damping parameter (α) compared to that of YIG, owing to the additional relaxation mechanisms from the large spin-orbit coupling of the rare earth ions.[61,62] Values of the Gilbert damping parameter for thulium iron garnet (TmIG) and europium iron garnet (EuIG) have been reported as on the order of $\alpha \approx 10^{-3}$ and $\approx 10^{-2}$, respectively.[18,19,63] The DyIG film yielded a value of $\alpha = 0.23 \pm 0.02$. This value is considerably higher than that of EuIG and TmIG, but corresponds well with measurements on bulk REIG samples where DyIG was found to have damping roughly an order of magnitude higher than both EuIG and TmIG.[64]

The depth dependence of the nuclear structure and in-plane component of the magnetization were obtained from fits to room temperature measurements of the polarized neutron reflectivity (PNR, Figure S2, Supporting Information) in a field of 700 mT, as shown in Figure 1c for a 116 nm-thick DyIG/GGG film. The magnetic moment of neutrons and the specular reflection geometry of PNR measurements provide depth-dependent information on the in-plane component of magnetization, magnetic roughness, density, and interfacial roughness.[65] The reflectometry curves are fit to a structural model, from which the scattering length density (SLD) is extracted. The nuclear SLD is sensitive to density and composition. It shows that there is a gradient of the composition of the DyIG, and a region near the DyIG/GGG interface with a SLD smaller than the theoretical value for bulk DyIG. This gradient and low SLD can be caused by a Fe-depleted interface which is proposed to be a result of Ga or Gd from the GGG substituting into the Fe sites, as seen in other iron garnets grown on GGG substrates.[66,67] Near the top surface, the DyIG has a SLD consistent with bulk calculations. The magnetic SLD data show that the magnetization of the DyIG is 59.8 ± 5.5 kA m^{-1} in agreement with VSM data, and the fit gives a 1.6 nm nonmagnetic layer at both the top and bottom of the DyIG. The top nonmagnetic layer is assumed to be a result of surface roughness, which is also seen in the nuclear SLD and is also present

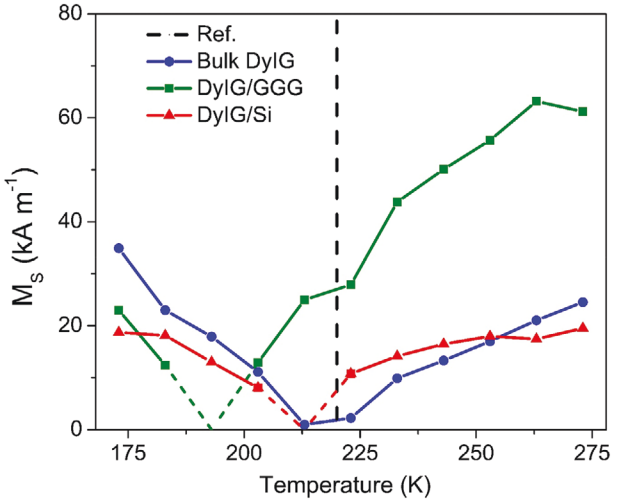

Figure 2. Magnetic moment versus temperature for bulk DyIG, DyIG/GGG, and DyIG/Si samples. The vertical dashed line indicates the literature value of the magnetic compensation temperature. Solid lines are experimental data; the red and green dashed lines indicate interpolation due to the divergent coercive field.

in polycrystalline films, Figure S6a, Supporting Information. The bottom nonmagnetic layer corresponds to Ga or Gd interdiffusion or local intermixing.

3. Polycrystalline DyIG on Si

DyIG films of 22–39 nm thickness were grown on Si (100) and underwent a rapid-thermal anneal (RTA) at 750–950 °C for 5 min to crystallize them from the amorphous as-grown state. Grazing incidence x-ray diffraction (XRD) scans (**Figure 3**a) showed no evidence of secondary phases across the range of thicknesses, and XRD pole figures showed garnet peaks with no evidence of a preferred crystallographic orientation. X-ray photoelectron spectroscopy showed that the Dy:Fe ratio in the film matched that of the DyIG target material. Dy^{3+} was the only observed valence state for dysprosium, and the iron valence states could not be resolved.

PNR was also collected for a 40 nm DyIG/Si film, with the SLD profiles show in Figure 3b, collected at room temperature in a field of 700 mT (see Figure S3, Supporting Information). In the nuclear and magnetic SLD profile, the interface near the substrate and DyIG layers is smeared, which is indicative of intermixing between the layers. The SLD provided by PNR represents an average across the sample plane, so the technique cannot determine if the intermixing at the interface originates from interfacial diffusion or local roughness. However, the apparent penetration of the magnetic SLD into the Si layer does not indicate proximity magnetism, but simply mirrors the interfacial mixing. The interfacial region at the substrate likely corresponds to the dysprosium-rich region detected at the interface via electron energy loss spectroscopy (EELS, see Figure S6, Supporting Information). The magnetic SLD data confirm the saturation magnetization value obtained from VSM measurements. As in the DyIG/GGG case, neutron imaginary SLD is minimal.

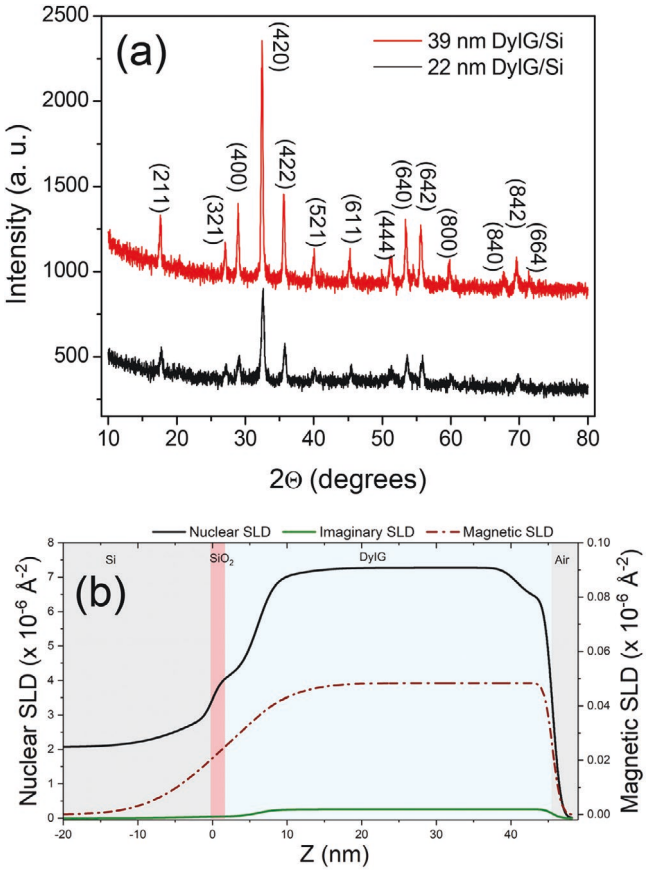

Figure 3. a) 2Θ grazing incidence x-ray diffraction scans of DyIG/Si thin films (vertically offset for clarity). No secondary phases are present in the films. b) Nuclear (black, solid), imaginary SLD (green, solid), and magnetic (red, dashed) SLD as a function of depth as determined from fitting PNR data (see Figure S3, Supporting Information), where $z = 0$ nm refers to the surface of the Si substrate.

Atomic force microscopy (AFM) measurements demonstrate sub-nanometer RMS roughness of 0.7–0.9 nm and an exceptionally large grain size of 5–10 μm with a radiating groove pattern for certain growth and annealing conditions (see **Figure 4**a for a representative image of a 38 nm thick film annealed at 950 °C). The radiating groove pattern is evident in the AFM images but the amplitude of the grooves is below 1 nm. The grain boundaries are straight and scans on multiple areas of the sample reveal all grains had similar sizes, indicating that a site-saturated nucleation occurred during the annealing step.[68] To investigate this further, we annealed films of 20 and 40 nm nominal thicknesses at a variety of temperatures from 550–950 °C. 750 °C was the minimum temperature for which pure phase garnet was obtained, and films annealed below this temperature contained at least a minority $DyFeO_3$ orthoferrite phase. Films annealed at 750 °C had grain sizes on the order of ≈100 nm (obtained from the XRD peak width), comparable to EuIG/quartz films.[23] For films of roughly 40 nm thickness, large grains were obtained for temperatures above 850 °C, but there was little dependence of grain size on temperature in the range of 850–950 °C.

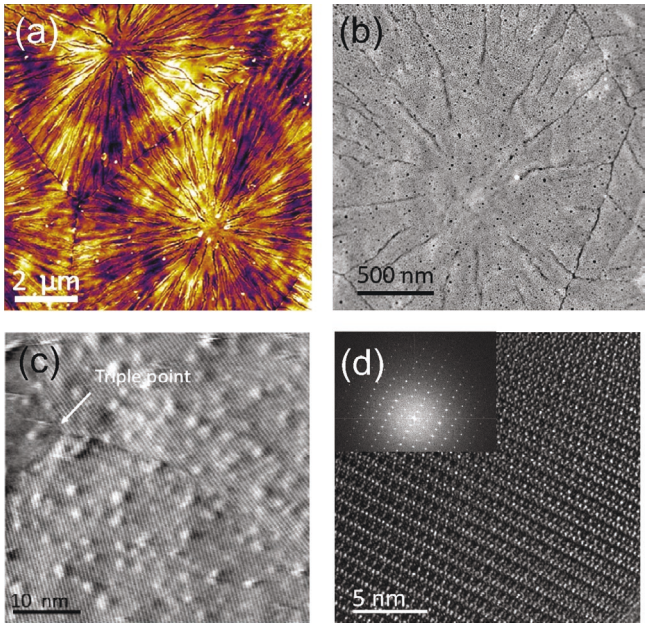

Figure 4. a) AFM scan of a 38 nm DyIG/Si sample annealed at 950 °C. Grains on the order of 10 μm across can be seen, along with a radiating grooved pattern originating from the center of the grains. b) ADF-STEM image of a 22 nm DyIG sample grown on a 200 nm Si_3N_4 membrane in plane-view showing grain boundaries and radiating grooves. c) Image near a triple point of the plane-view sample showing lattice fringes in two of the grains. d) HR-TEM image of a DyIG film obtained in cross-section showing the fringes corresponding to its lattice spacing. Inset shows the FFT from the image.

Scanning transmission electron microscopy (STEM) analysis was performed in plane-view on a 22 nm DyIG film grown directly on a Si_3N_4 membrane. Figure 4b is a low magnification annular dark-field (ADF)-STEM image in which the radiating groove patterns can be seen. The grooves are not aligned along specific crystallographic directions and most likely represent height differences originating from a surface instability during grain growth. They do not correspond to dislocations or other defects with the grains and the lattice fringes are continuous across them (Figure S5d, Supporting Information). Figure 4c shows an ADF-STEM image of the sample showing three grains meeting at a triple point. Two grains shows lattice fringes which extend to the grain boundary, indicating that there is no significant disordered region separating the grains. Figure S5a,b, Supporting Information, shows Kikuchi lines within the grains and a diffraction pattern consisting of discrete spots from a region of the sample containing two or three grains, again illustrating the large grain size and excellent crystal quality of the film.

Figure 4d shows a high resolution (HR)-TEM image from a 41 nm DyIG film on an oxidized silicon substrate, in cross-section, that was prepared using focused ion beam (FIB). A periodic lattice is clearly observed, with no visible dislocations or other defects. To reveal the distribution of Dy and Fe along the thickness of the film, EELS was also performed. A small Dysprosium-rich region at the substrate interface was observed but the Dy:Fe ratio was constant throughout the remaining film thickness (Figure S6, Supporting Information). The higher Dy:Fe ratio at the substrate may be a result of Fe diffusion into the substrate during growth or annealing, and may

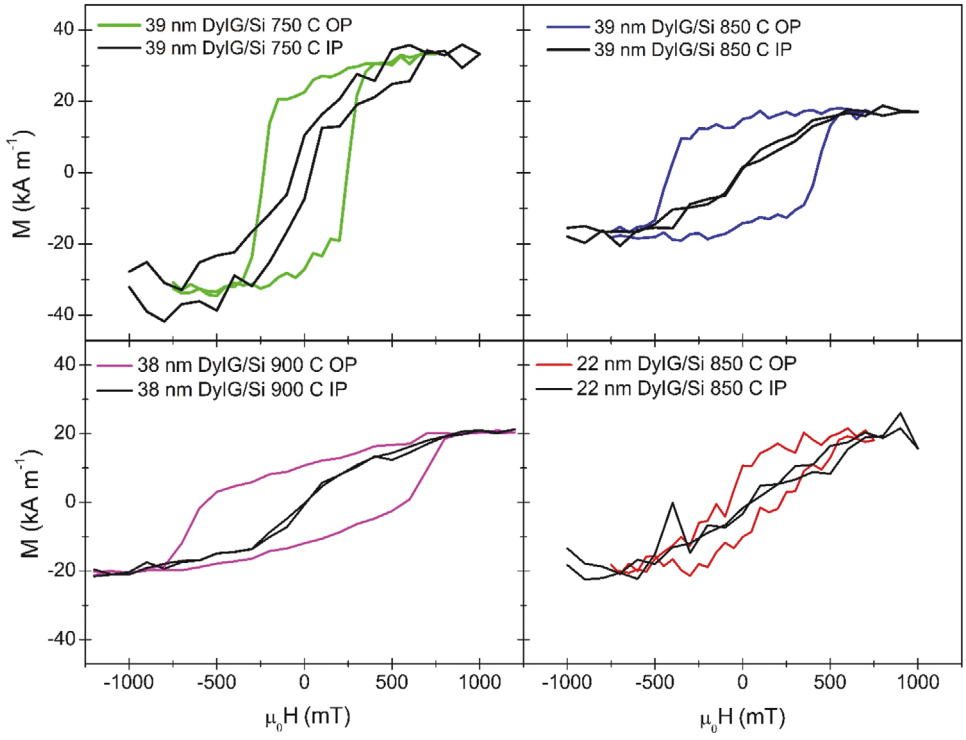

Figure 5. VSM hysteresis loops of DyIG/Si samples of selected thicknesses and annealing temperatures. IP and OP refer to the field direction during the measurement. All samples have an OP easy axis.

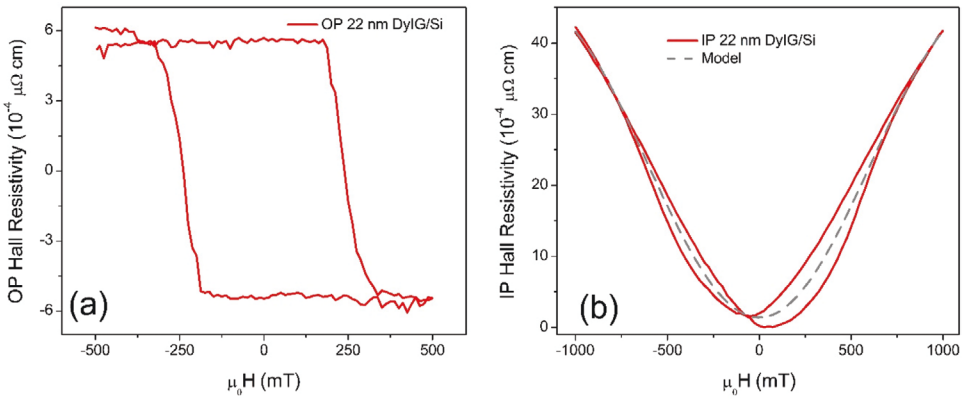

Figure 6. a) Out of plane AHE-like SMR on a Pt(4 nm)/DyIG (22 nm)/Si Hall bar). b) In plane SMR loop on the same device. The dashed line is a fit to a macrospin model.

be compared with the gradient in the calculated SLD for the epitaxial DyIG/GGG and polycrystalline DyIG/Si samples.

As seen in **Figure 5**, polycrystalline DyIG films grown on Si demonstrate PMA with high out-of-plane remanence. M_s ranges from ≈20–30 kA m^{-1}, close to the bulk value of 31 kA m^{-1},[58] and was highest for films annealed at 750 °C. In Figure 5a–c, as the annealing temperature increased from 750 to 900 °C, the coercivity of the OP loop increased from ≈250–600 mT.

The net uniaxial anisotropy of the polycrystalline film is given by

$$K_{u,pc} = -\frac{3}{2}\lambda\frac{E}{1-\nu}\Delta\alpha_T\Delta T - \frac{\mu_0}{2}M_s^2 \quad (2)$$

where λ is the average magnetostriction for a polycrystal, E is the elastic modulus, ν is Poisson's ratio, $\Delta\alpha_T$ is the difference in thermal expansion coefficients between the film and substrate, and ΔT is the temperature change from the annealing temperature to room temperature. The λ is an appropriate average of the two cubic magnetostriction coefficients λ_{100} and λ_{111},[23,69] $\lambda = 0.4\lambda_{100} + 0.6\lambda_{111}$ with $\lambda_{100} = -12.5 \times 10^{-6}$.[15] We use Equation[2] to estimate the anisotropy field, assuming the thermal expansion coefficients of DyIG are constant over the temperature range of interest ($\alpha = 7.50 \times 10^{-6}$ K^{-1} over the range 220–450 K).[70] This is justified by the insignificant change in the value of α over the temperature interval of 296–1399 K for YIG.[43] For Si, α is integrated over the temperature range of interest.[71] For the film in Figure 5a, with the lowest annealing temperature of 750 °C and highest M_s,[72,73] Equation (2) results in a value for the estimated anisotropy fields of 0.53 T, rising to 0.96 and 1.01 T for the films annealed at 850 and 900 °C. This qualitatively agrees with the expectation that anisotropy field should scale with strain, and therefore annealing temperature. The anisotropy in the polycrystalline films is expected to be higher than that of the single crystal films due to the greater strain state. Moreover, the grain boundaries can act as domain wall pinning sites explaining the higher coercivity.

The compensation temperature of a polycrystalline DyIG/Si sample was ≈220 K, similar to the bulk sample but different from the DyIG/GGG sample grown at the same time. We hypothesize that the difference may relate to cation site occupancy in the polycrystalline film that is closer to bulk due to the high annealing temperature.

To gauge the potential of DyIG/Si films as spintronic devices, we patterned Pt/DyIG/Si into Hall bar heterostructures and conducted spin Hall magnetoresistance (SMR) measurements. The SMR-induced anomalous Hall effect (AHE) resistance obtained in an applied out-of-plane magnetic field is shown in **Figure 6**a for a Pt(4 nm)/DyIG (22 nm)/Si Hall bar. A sample-dependent offset and a linear background from the ordinary Hall effect (OHE) of Pt were subtracted from the raw data. The film shows sharp magnetization reversal at ≈250 mT, significantly larger than the ≈100 mT coercivity of the unpatterned film. We attribute this difference to differences in geometry or strain state of the patterned structure versus the unpatterned film. The amplitude of the AHE loop (11.0×10^{-4} μΩ cm) is close in magnitude to that measured for other garnet/Pt heterostructures including EuIG, TbIG, and TmIG.[2,19,23] The IP SMR loop could not be completely saturated in our experimental setup. However, a fit to a macrospin model produced an anisotropy field of 1.2 T and an IP SMR amplitude of 42.4×10^{-4} μΩ cm with a good fit to the experimental data. By neglecting the real part of the spin mixing conductance (G_r) in the model of Chen et al.[74] for SMR, we are able to obtain a lower bound on the imaginary part of the spin mixing conductance (G_i) of 1.05×10^{13} Ω^{-1} m^{-2}. If we use the IP SMR amplitude obtained from the macrospin model fit to the data, we obtain a G_i value approximately 11% larger, indicating that the approximation is reasonable.

4. Conclusion

We have demonstrated the growth of large grained, single phase DyIG films on Si substrates with PMA. The DyIG/Si samples exhibit saturation magnetization and a magnetic compensation temperature close to the bulk value, and a coercivity and anisotropy field dependent on the annealing temperature. PMA originates from magnetoelastic anisotropy due to the thermal mismatch strain. Spin transport measurements show that the AHE-like SMR and spin mixing conductance at the Pt/DyIG interface are similar to other Pt/single crystal REIG and Pt/polycrystalline EuIG/quartz heterostructures, indicating that Pt/DyIG on Si has high interfacial spin transparency. Single

crystal DyIG films were grown for comparison with the polycrystalline DyIG, showing control over anisotropy in a wide range via lattice mismatch strain, low coercivity, but higher Gilbert damping than EuIG and TmIG.

These results establish DyIG as a promising platform for Si-integrated spintronic devices, provided that annealing temperatures can be lowered to maintain compatibility with back-end processes, e.g. by using local laser annealing.[75] The ability to tune the anisotropy, the high spin mixing conductance, and the large grain sizes are favorable attributes for the complex demands of spintronic devices. As the garnet structure easily accommodates cation substitutions, compositions of $Dy_xY_{3-x}Fe_5O_{12}$ may allow further optimization by leveraging the benefits of the high magnetostriction of DyIG and the low Gilbert damping of YIG.

5. Experimental Section

DyIG films were grown by pulsed laser deposition from a stoichiometric DyIG target produced by solid oxide sintering methods.[76] The laser used was a 248 nm KrF excimer laser with a repetition rate of 10 Hz, a pulse energy of 400 mJ, and a substrate to target distance of 8 cm. All films were grown at a substrate temperature of 650 °C and an oxygen pressure of 150 mTorr. Films on garnet substrates were studied without further annealing. The amorphous as-grown films on Si (100) substrates were annealed ex situ for 5 min in temperatures from 750–900 °C to induce crystallization. Pt (4 nm) was deposited on the DyIG films by DC magnetron sputtering and patterned into Hall cross structures (620 µm by 50 µm) using photolithography and ion milling.

Film crystallinity for the samples on Si substrates was investigated with a Rigaku Smartlab XRD with a Cu Kα source using grazing incidence x-ray diffraction (GIXD) and the with the films deliberately rotated to minimize the contribution of the substrate.[77] Samples on garnet substrates were measured by high-resolution XRD (HRXRD) and film thickness was determined from x-ray reflectivity (XRR) using a Bruker D8 Discover with a Cu Kα source.[77] Atomic force microscopy (AFM) measurements to determine surface roughness and topography were obtained using an Asylum Research AFM with Bruker OTESPA-R3 tips.[77] Magnetic hysteresis loops were measured on a Digital Measurements Systems Vibrating Sample Magnetometer (VSM) Model 1660.[77] SMR measurements were conducted using a standard lock-in technique.[2] FMR was collected using a Giga-tronics 12000A Series Microwave Synthesizer and a custom waveguide.[77]

PNR was collected using the Polarized Beam Reflectometer instrument at the National Institute of Standards and Technology Center for Neutron Research. The incident neutrons were spin-polarized parallel or antiparallel to the magnetic field (H), and the reflectivity was measured in the non-spin-flip cross sections (R^{++} and R^{--}) as a function of the momentum transfer (Q) normal to the surface of the film. PNR measurements were taken at room temperature with a magnetic field of 700 mT applied in the plane of the sample. The PNR data were reduced and modeled, to a $\chi^2 = 1.55$, using the REDUCTUS and REFL1D software packages, respectively.[78,79]

Sample preparation for STEM analysis was carried out using FEI Helios Nanolab G4 dual-beam FIB. Aberration-corrected FEI Titan G2 60–300 STEM equipped with a CEOS DCOR probe corrector, a Schottky extreme field emission gun, a monochromator, and a Gatan Enfinium ER spectrometer were used.[77] The microscope was operated at 200 kV, 25.5 mrad probe convergence semi-angle, and a 77 mm camera length for EELS. A band pass filter (pass band 0.7–10 Å) was applied to improve lattice visibility and reduce the noise. Samples were prepared for analysis in plane-view and cross-section. To obtain plane view images, a DyIG film was grown onto a 200 nm Si_3N_4 membrane which then was FIB-cut into about 50×20 µm^2 rectangular section and transferred onto a Cu half grid for STEM analysis. The cross-sectional samples were FIB-cut from a DyIG film grown onto an oxidized silicon substrate.

Supporting Information

Supporting Information is available from the Wiley Online Library or from the author.

Acknowledgements

The authors acknowledge support of SMART, a Center of nCORE sponsored by SRC and NIST, and NSF DMR 1808190. This work made use of the Shared Experimental Facilities at MIT supported in part by the MRSEC Program of the National Science Foundation under award number DMR – 1419807. The authors also acknowledge the support of DARPA under award number HR0011834375. STEM analysis was performed in the Characterization Facility of the University of Minnesota, which receives partial support from the NSF through the MRSEC program.

Conflict of Interest

The authors declare no conflict of interest.

Keywords

magnetic insulators, oxides, silicon, spintronics

Received: August 3, 2019
Revised: November 4, 2019
Published online: November 28, 2019

[1] Y. Kajiwara, K. Harii, S. Takahashi, J. Ohe, K. Uchida, M. Mizuguchi, H. Umezawa, H. Kawai, K. Ando, K. Takanashi, S. Maekawa, E. Saitoh, *Nature* **2010**, *464*, 262.
[2] C. O. Avci, A. Quindeau, C. F. Pai, M. Mann, L. Caretta, A. S. Tang, M. C. Onbasli, C. A. Ross, G. S. D. Beach, *Nat. Mater.* **2017**, *16*, 309.
[3] M. Montazeri, P. Upadhyaya, M. C. Onbasli, G. Yu, K. L. Wong, M. Lang, Y. Fan, X. Li, P. K. Amiri, R. N. Schwartz, C. A. Ross, K. L. Wang, *Nat. Commun.* **2015**, *6*, 8958.
[4] J. Li, G. Yu, C. Tang, Y. Liu, Z. Shi, Y. Liu, A. Navabi, M. Aldosary, Q. Shao, K. L. Wang, R. Lake, J. Shi, *Phys. Rev. B* **2017**, *95*, 241305 (R).
[5] L. J. Cornelissen, J. Liu, R. A. Duine, J. Ben Youssef, B. J. Van Wees, *Nat. Phys.* **2015**, *11*, 1022.
[6] A. Hamadeh, O. D'Allivy Kelly, C. Hahn, H. Meley, R. Bernard, A. H. Molpeceres, V. V. Naletov, M. Viret, A. Anane, V. Cros, S. O. Demokritov, J. L. Prieto, M. Muñoz, G. De Loubens, O. Klein, *Phys. Rev. Lett.* **2014**, *113*, 197203.
[7] L. Soumah, N. Beaulieu, L. Qassym, C. Carrétéro, E. Jacquet, R. Lebourgeois, J. Ben Youssef, P. Bortolotti, V. Cros, A. Anane, *Nat. Commun.* **2018**, *9*, 3355.
[8] M. Schreier, T. Chiba, A. Niedermayr, J. Lotze, H. Huebl, S. Geprägs, S. Takahashi, G. E. W. Bauer, R. Gross, S. T. B. Goennenwein, *Phys. Rev. B* **2015**, *92*, 144411.
[9] L. Bi, J. Hu, P. Jiang, D. H. Kim, G. F. Dionne, L. C. Kimerling, C. A. Ross, *Nat. Photonics* **2011**, *5*, 758.
[10] T. Fakhrul, S. Tazlaru, L. Beran, Y. Zhang, M. Veis, C. A. Ross, *Adv. Opt. Mater.* **2019**, *7*, 1900056.
[11] T. Yoshimoto, T. Goto, R. Isogai, Y. Nakamura, H. Takagi, C. A. Ross, M. Inoue, *Opt. Express* **2016**, *24*, 8746.
[12] S. Geller, H. J. Williams, R. C. Sherwood, J. P. Remeika, G. P. Espinosa, *Phys. Rev.* **1963**, *131*, 1080.

[13] S. Geller, J. P. Remeika, R. C. Sherwood, H. J. Williams, G. P. Espinosa, *Phys. Rev.* **1965**, *137*, A1034.
[14] R. F. Pearson, *J. Appl. Phys.* **1962**, *33*, 1236.
[15] S. Iida, *J. Phys. Soc. Jpn.* **1967**, *22*, 1201.
[16] H. Chang, P. Li, W. Zhang, T. Liu, A. Hoffmann, L. Deng, M. Wu, *IEEE Magnetics Letters* **2014**, *5*, 1.
[17] C. L. Jermain, H. Paik, S. V. Aradhya, R. A. Buhrman, D. G. Schlom, D. C. Ralph, *Appl. Phys. Lett.* **2016**, *109*, 192408.
[18] A. Quindeau, C. O. Avci, W. Liu, C. Sun, M. Mann, A. S. Tang, M. C. Onbasli, D. Bono, P. M. Voyles, Y. Xu, J. Robinson, G. S. D. Beach, C. A. Ross, *Adv. Electron. Mater.3*, **2017**, 1600376.
[19] E. R. Rosenberg, L. Beran, C. O. Avci, C. Zeledon, B. Song, C. Gonzalez-Fuentes, J. Mendil, P. Gambardella, M. Veis, C. Garcia, G. S. D. Beach, C. A. Ross, *Phys. Rev. Mater.* **2018**, *2*, 094405.
[20] M. Duan, A. M. Grishin, K. V. Rao, T. Suzuki, *IEEE Transactions Magn.* **1995**, *31*, 3245.
[21] N.. Ibrahim, C. Edwards, S.. Palmer, *J. Magn. Magn. Mater.* **2000**, *220*, 183.
[22] P. Hansen, J. P. Krumme, *Thin Solid Films* **1984**, *114*, 69.
[23] J. J. Bauer, E. R. Rosenberg, C. A. Ross, *Appl. Phys. Lett.* **2019**, *114*, 052403.
[24] M. Shalaby, F. Vidal, M. Peccianti, R. Morandotti, F. Enderli, T. Feurer, B. D. Patterson, *Phys. Rev. B* **2013**, *88*, 140301 (R).
[25] S. Mangin, D. Ravelosona, J. A. Katine, E. E. Fullerton, *INTERMAG 2006 – IEEE Int. Magn. Conf.* **2006**, *5*, 5.
[26] D. Apalkov, B. Dieny, J. M. Slaughter, *Proc. IEEE* **2016**, *104*, 1796.
[27] N. Vlietstra, J. Shan, V. Castel, B. J. Van Wees, J. Ben Youssef, *Phys. Rev. B* **2013**, *87*, 184421.
[28] Y. Fan, P. Upadhyaya, X. Kou, M. Lang, S. Takei, Z. Wang, J. Tang, L. He, L. Te Chang, M. Montazeri, G. Yu, W. Jiang, T. Nie, R. N. Schwartz, Y. Tserkovnyak, K. L. Wang, *Nat. Mater.* **2014**, *13*, 699.
[29] J. Han, A. Richardella, S. A. Siddiqui, J. Finley, N. Samarth, L. Liu, *Phys. Rev. Lett.* **2017**, *119*, 077702.
[30] K. Garello, C. O. Avci, I. M. Miron, M. Baumgartner, A. Ghosh, S. Auffret, O. Boulle, G. Gaudin, P. Gambardella, *Appl. Phys. Lett.* **2014**, *105*, 212402.
[31] L. Liu, C. F. Pai, H. W. Tseng, D. C. Ralph, R. A. Buhrman, *Science* **2012**, *336*, 555.
[32] N. Sato, F. Xue, R. M. White, C. Bi, S. X. Wang, *Nat. Electron.* **2018**, *1*, 508.
[33] H. Yamahara, M. Mikami, M. Seki, H. Tabata, *J. Magn. Magn. Mater.* **2011**, *323*, 3143.
[34] V. H. Ortiz, M. Aldosary, J. Li, Y. Xu, M. I. Lohmann, P. Sellappan, Y. Kodera, J. E. Garay, J. Shi, *APL Mater.*. **2018**, *6*, 121113.
[35] M. Kubota, K. Shibuya, Y. Tokunaga, F. Kagawa, A. Tsukazaki, Y. Tokura, M. Kawasaki, *J. Magn. Magn. Mater.* **2013**, *339*, 63.
[36] C. Tang, P. Sellappan, Y. Liu, Y. Xu, J. E. Garay, J. Shi, *Phys. Rev. B* **2016**, *94*, 140403 (R).
[37] E. Popova, N. Keller, F. Gendron, L. Thomas, M.-C. Brianso, M. Guyot, M. Tessier, S. S. P. Parkin, *J. Vac. Sci. Technol., A* **2001**, *19*, 2567.
[38] L. G. Van Uitert, E. M. Gyorgy, W. A. Bonner, W. H. Grodkiewicz, E. J. Heilner, G. J. Zydzik, *Mater. Res. Bull.* **1971**, *6*, 1185.
[39] Y. Hosoe, R. Imura, R. Suzuki, T. Ikeda, *IEEE Trans. Magn.* **1989**, *25*, 4254.
[40] A. N. Shaposhnikov, A. R. Prokopov, V. N. Berzhansky, A. V. Karavainikov, Y. E. Vysokikh, N. N. Gerasimenko, D. I. Smirnov, *Mater. Res. Bull.* **2017**, *95*, 115.
[41] Y. Zhang, Q. Du, C. Wang, W. Yan, L. Deng, J. Hu, C. A. Ross, L. Bi, *APL Mater.*. **2019**, *7*, 081119.
[42] M. Kuila, Z. Hussain, V. R. Reddy, *J. Magn. Magn. Mater.* **2019**, *473*, 458.
[43] S. Geller, G. P. Espinosa, P. B. Crandall, *J. Appl. Crystallogr.* **1969**, *2*, 86.
[44] J. P. Sutter, H. Yavaş, *arXiv* **2016**, arXiv:1612.07049.
[45] K. A. Hussain, D. B. Sirdeshmukh, *Cryst. Res. Technol.* **1993**, *28*, 1147.
[46] S. Mito, J. Kim, K. H. Chung, H. Takagi, M. Inoue, *IEICE Trans. Electron.* **2009**, *E92-C*, 1487.
[47] I. L. Snetkov, A. I. Yakovlev, D. A. Permin, S. S. Balabanov, O. V. Palashov, *Opt. Lett.* **2018**, *43*, 4041.
[48] A. E. Clark, E. Callen, *J. Appl. Phys.* **1968**, *39*, 5972.
[49] M. Lahoubi, A. Bouguerra, A. Kihal, G. Fillion, *J. Alloys Compd.* **1998**, *275-277*, 598.
[50] M. Lahoubi, W. Younsi, M. L. Soltani, B. Ouladdiaf, *J. Phys.: Conf. Ser.* **2010**, *200*, 082018.
[51] A. Boutaba, M. Lahoubi, V. Varazashvili, S. Pu, *J. Supercond. Nov. Magn.* **2019**, https://doi.org/10.1007/s10948-019-5025-4.
[52] V. Ram Yadav, H. B. Lal, *Jpn. J. Appl. Phys.* **1979**, *18*, 2229.
[53] M. A. Ahmed, S. T. Bishay, S. I. El-Dek, *Mater. Chem. Phys.* **2011**, *126*, 780.
[54] V. A. Kotov, V. G. Shavrov, A. F. Popkov, M. Vasiliev, K. Alameh, M. Nur-E-Alam, L. N. Alyabyeva, D. E. Balabanov, V. I. Burkov, M. K. Virchenko, *J. Nanomater.* **2018**, *2018*, 1.
[55] J. Ostorero, M. Guillot, *IEEE Trans. Magn.* **2004**, *40*, 2823.
[56] G. P. Espinosa, *J. Chem. Phys.* **1962**, *37*, 2344.
[57] Y. A. Burenkov, S. P. Nikanorov, *Phys. Solid State* **2002**, *44*, 318.
[58] A. Paoletti, *Physics of Magnetic Garnets*, North-Holland Pub. Co., Amsterdam **1979**.
[59] D. Hunter, W. Osborn, K. Wang, N. Kazantseva, J. Hattrick-Simpers, R. Suchoski, R. Takahashi, M. L. Young, A. Mehta, L. A. Bendersky, S. E. Lofland, M. Wuttig, I. Takeuchi, *Nat. Commun.* **2011**, *2*, 518.
[60] R. Pauthenet, *J. Appl. Phys.* **1959**, *30*, S290.
[61] J. H. Van Vleck, *J. Appl. Phys.* **1964**, *35*, 882.
[62] H. Maier-Flaig, S. Klingler, C. Dubs, O. Surzhenko, R. Gross, M. Weiler, H. Huebl, S. T. B. Goennenwein, *Phys. Rev. B* **2017**, *95*, 214423.
[63] C. N. Wu, C. C. Tseng, Y. T. Fanchiang, C. K. Cheng, K. Y. Lin, S. L. Yeh, S. R. Yang, C. T. Wu, T. Liu, M. Wu, M. Hong, J. Kwo, *Sci. Rep.* **2018**, *8*, 11087.
[64] G. P. Vella-Coleiro, D. H. Smith, L. G. Van Uitert, *Appl. Phys. Lett.* **1972**, *21*, 36.
[65] H. Zabel, K. Theis-Brohl, *J. Phys.: Condens. Matter* **2003**, *15*, S505.
[66] J. F. K. Cooper, C. J. Kinane, S. Langridge, M. Ali, B. J. Hickey, T. Niizeki, K. Uchida, E. Saitoh, H. Ambaye, A. Glavic, *Phys. Rev. B* **2017**, *96*, 104404.
[67] A. Mitra, O. Cespedes, Q. Ramasse, M. Ali, S. Marmion, M. Ward, R. M. D. Brydson, C. J. Kinane, J. F. K. Cooper, S. Langridge, B. J. Hickey, *Sci. Rep.* **2017**, *7*, 11774.
[68] C. V. Thompson, R. Carel, *J. Mech. Phys. Solids* **1996**, *44*, 657.
[69] N. S. Akulov, *Zeitschrift für Physik* **1930**, *66*, 533.
[70] A. Budkowski, A. Szytuła, D. Rodic, R. Duraj, J. Mayer, J. Sciesinski, V. Spasojevic, *J. Magn. Magn. Mater.* **1989**, *78*, 226.
[71] Y. Okada, Y. Tokumaru, *J. Appl. Phys.* **1984**, *56*, 314.
[72] T. B. Bateman, *J. Appl. Phys.* **1966**, *37*, 2194.
[73] N. S. Sokolov, V. V Fedorov, A. M. Korovin, S. M. Suturin, D. A. Baranov, S. V Gastev, B. B. Krichevtsov, K. Yu, *J. Appl. Phys.* **2016**, *119*, 023903.
[74] Y.-T. Chen, S. Takahashi, H. Nakayama, M. Althammer, S. T. B. Goennenwein, E. Saitoh, G. E. W. Bauer, *Phys. Rev. B* **2013**, *87*, 144411.
[75] D. A. Herman, J. C. Deluca, H. J. Vollmer, *J. Appl. Phys.* **1981**, *52*, 2341.
[76] T. Goto, M. C. Onbaşlò, C. A. Ross, *Opt. Express* **2012**, *20*, 28507.
[77] Certain commercial equipment and instruments are identified in this paper to foster understanding. Such identification does not imply recommendation or endorsement by the National Institute of Standards and Technology, nor does it imply that the equipment identified are necessarily the best available for the purpose.
[78] B. J. Kirby, P. A. Kienzle, B. B. Maranville, N. F. Berk, J. Krycka, F. Heinrich, C. F. Majkrzak, *Curr. Opin. Colloid Interface Sci.* **2012**, *17*, 44.
[79] P. A. Kienzle, B. B. Maranville, K. V. O'Donovan, J. F. Ankner, N. F. Berk, C. F. Majkrzak, "Reflectometry Software," https://www.nist.gov/ncnr/reflectometry-software **2017**.

